

Numerical Full Inversion of Two Dielectric Cylinders upon a Metallic Plane: A First Step toward Forest Parameters Retrieval from VHF to P-Band Radar Data

Cyril Dahon^{1, 2, *}, Alonso Cano^{1, 2}, Mandiaye Fall^{1, 2},
Guillaume Marrelec³, and Gilles Chardon⁴

Abstract—Radar remote sensing applied to forest covers is a domain of interest for a few decades, particularly in forest monitoring for the global carbon cycle. In this paper, we use a numerical electromagnetic scattering model to investigate the full-inversion of a simple case where two dielectric cylinders are lying upon a metallic ground seen as a theoretical representation of only one tree trunk and one primary branch. The presented process performs cylinders 3D-locations estimation using an Orthogonal Matching Pursuit (OMP) algorithm, then scattering coefficient is retrieved for each cylinder and each scattering mechanism separately and finally the cylinders biophysical parameters (height, radius, complex permittivity) inversion using a Particle Swarm Optimisation (PSO) algorithm. This process is based on target subspace decomposition and applied to noisy simulated radar data.

1. INTRODUCTION

Radar remote sensing applied to forest covers has been a domain of interest for a few decades, particularly in forest monitoring for the global carbon cycle through the aboveground biomass evaluation [1, 2] or in foliage penetration (FOPEN) applications [3, 4].

On one hand, several measurement techniques have been investigated from Polarimetric [5] and/or interferometric sensors [6, 7] to data fusion such as RADAR/LIDAR data [8], from high resolution SAR imaging [9] to tomography [10–12]. All of them consist in top-down approaches, aiming to extract biophysical information from real data acquired on real forest at large geographic scale: from forest stand scale [13] to the continental scale [14]. But a real forest stand is a very complex medium from an electromagnetic point of view, strongly impacting the inversion methods.

On the other hand, a complementary approach has been followed through numerical forest models to help radar images interpretations or measurement configurations setup. There are several kinds of physical models, from empirical approaches [15] to numerical electromagnetic scattering models. Among the latter, we can find incoherent models such as [16] and coherent ones such as [17]. Both kinds rely on electromagnetic approximations to allow forest stands modelling. Another class of electromagnetic models relies on numerical solutions of the electric-field integral equation using the Method of Moments such as [18–20]. More recently, the latter model has been updated [21, 22] to be able to solve large electromagnetic problems in a reasonable delay. Numerical models have then proven their ability to be useful tools to develop inversion methods.

Received 9 February 2022, Accepted 19 May 2022, Scheduled 10 June 2022

* Corresponding author: Cyril Dahon (cyril.dahon@upmc.fr).

¹ Sorbonne Université, CNRS, Laboratoire de Génie Électrique et Électronique de Paris, Paris 75252, France. ² Université Paris-Saclay, CentraleSupélec, CNRS, Laboratoire de Génie Électrique et Électronique de Paris, Gif-sur-Yvette 91192, France. ³ Sorbonne Université, CNRS, INSERM, Laboratoire d'imagerie biomédicale, LIB, F-75006, Paris, France. ⁴ Université Paris-Saclay, CNRS, CentraleSupélec, Laboratoire des signaux et systèmes, Gif-sur-Yvette 91190, France.

This paper aims to investigate this ability. Using an approximate scattering model ([23, 24] already used in [17]), we attempt to build a full-inversion process for a low complexity problem which is intended to be increased step by step. We have chosen to develop an inversion process able to first solve the source localization problem (3-D imaging), then perform the electromagnetic inversion (scattering coefficients), and finally operate the biophysical inversion (cylinders parameters).

The localization problem is formulated as a sparse approximation problem: each possible position of an object is represented by a linear subspace, modeling the field scattered by the object, taking into account the diversity of biophysical parameters. The full scattered field can then be represented as a sparse sum of elementary scattered fields taken from the subspaces associated with the positions actually occupied by scatterers. The positions of the objects are then estimated using the Orthogonal Matching Pursuit algorithm, in its block-sparsity version.

Then the biophysical inversion is performed using a Particle Swarm Optimization process. This kind of algorithm is inspired by social animals' behavior [25] which have to find, for example, their meal in a complex surroundings by optimizing their expenditure of energy. Indeed, in our case, the cost functions have several local minima, and a single global minimum has to be found. A swarm is composed of a population of particles. The algorithm makes the particles evolve on the N -dimensional cost function surface through a velocity that updates the particle location (in fact its parameters set) at each iteration. Each particle velocity depends on the best location that it has previously found, as a "memory" effect. It depends too on the location found by any other particle which provided the minimum cost function value, as a "social" behavior.

At the "low" frequencies of interest (from UHF to P-band), the electromagnetic waves interact strongly under the canopy with trunks, primary branches, and the soil: scattering mechanisms involving multiple bounces are therefore of the first importance. As a first level of complexity, this paper presents a full-inversion process applied to the simple case where one vertical and one tilted dielectric cylinders are lying upon a metallic ground to model a tree trunk and a primary branch.

The radar data to inverse are simulated through a direct electromagnetic scattering model described in Section 2 whereas the inverse process relies on a direct modeling deconstruction approach described in Section 3. Direct modeling is used to perform a well-suited subspace decomposition (electromagnetic problem linearization) in Section 3.1 first to focalize 3D-images and locate the cylinders (Orthogonal Matching Pursuit algorithm) in Section 3.2, second to inverse the scattering complex coefficients of each cylinder in Section 3.3. Finally, a stochastic inverse technique based on direct modeling too (Particle Swarm Optimization) is used to estimate each cylinder biophysical parameters (height, radius, complex permittivity) in Section 3.4. Then Section 4 is dedicated to preliminary studies to highlight some specifications of the inversion process like the imaging zone translation, how to consider tilted cylinders and the target subspace size effect. Finally, the inversion process is applied to noisy (Section 5) simulated data, and the results are discussed. Section A.1 gathers all the parameters values used in the simulations and some comments on them.

Notice that this work is only a first attempt to answer the question from a theoretical and numerical point of view: is it possible to process a full inversion of simple tree components from numerical simulated data? And what would be the first prerequisites to do so? We have then chosen to study a non-real but numerically representative case of the elementary physics involved in more complex numerical forest models.

2. THE DIRECT PROBLEM FORMULATION

A direct "approximate" electromagnetic scattering model is used in two ways. First, it is an easy way to simulate radar data with a controlled ground truth. Second, the inversion algorithm introduced in this paper is based on its physical modeling approach.

2.1. The "Approximate" Scattering Model

The approximate scattering model relies on two levels of physical approximations.

First, at the scatterer level. The dielectric cylinder has to be long enough against the wavelength (infinite cylinder approximation [24]): Its scattered electric and magnetic fields are obtained in the

approximation of the infinite length cylinder and are used to calculate fictitious surface magnetic and electric currents. These fictitious surface currents are then the fictitious source of a finite height cylinder when the scattered (\mathbf{E}, \mathbf{H}) fields are calculated on a finite surface [23, 24]. This approximation allows an analytical solution for the scattering of a vertical lossy dielectric cylinder in free space, which can be translated and tilted through translation and Euler angles based rotation operator matrices. Computation is then very fast. The main drawback is the “infinite” cylinder approximation validity domain.

Second, at the forest level. To model a forest scene using this cylinder scattering model, we place a collection of scatterers (cylinders for branches and trunks [23, 24] and ellipsoids for leaves and needles [26] if needed) of different shapes and different orientations on a ground depending on tree species. Then we have to model the electromagnetic interaction between the incident wave and scatterers. Different levels of realism can be achieved, depending on which scattering mechanism is taken into account. This modular structure allows complex modeling for radar applications at forest scale [17] or simpler configurations for more fundamental studies.

In the case of a forest illuminated at low frequencies (UHF to P-band), the main contributions to radar signal come from trunks and primary branches. This is why an exemplary configuration with one vertical cylinder and an arbitrarily tilted one is on study in this paper.

2.2. The Physical “Forest” Model

At its lowest complexity level from an electromagnetic point of view, a forest stand can be reduced to a single dielectric cylinder lying upon a reflecting ground. The electromagnetic field scattered by such a target can be approximated to first order by four main scattering mechanisms (Figure 1). The single, the triple, and the double (“a” and “b”) bounces. The single bounce (SB) corresponds to the optic path of a propagating wave, from the emitting antenna to the scatterer and back to the receiving antenna (Figure 1(a)). The triple bounce (TB) corresponds to a wave impinging first on the ground, reflected toward the cylinder and then scattered back to the ground before reflecting again toward the receiving antenna (Figure 1(b)). The double bounce (DB) is a twin mechanism. The double bounce path “a” (DBa) corresponds to a wave path from the emitter to the cylinder and then scattered toward the ground where the wave reflects specularly toward the receiver (Figure 1(c)). The twin double bounce (DBb) is the inverse path, the wave interacting first with the ground and then with the cylinder (Figure 1(d)). This model assumes that the only scattering directions taken into account are those in the maximum of the local scattering pattern, namely in the forward, specular, and backward directions.

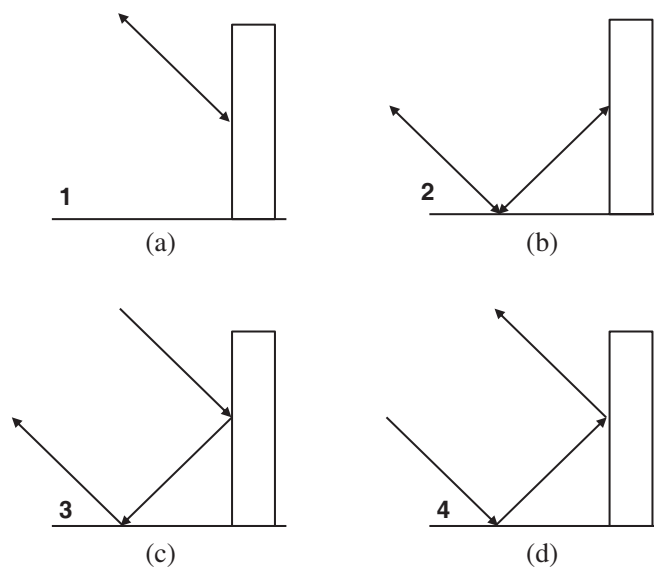


Figure 1. First order scattering mechanism interactions between a cylinder and the ground.

The mathematical formulation of such a model is:

$$\mathbf{E}_s^{\text{SB}} = \frac{e^{-jkr_s^{\text{SB}}}}{r_s^{\text{SB}}} \mathbf{S}_{\text{SB}} \frac{e^{-jkr_i^{\text{SB}}}}{r_i^{\text{SB}}} \mathbf{E}_i \quad (1)$$

$$\mathbf{E}_s^{\text{DBa}} = \frac{e^{-jkr_s^{\text{DBa}}}}{r_s^{\text{DBa}}} \mathbf{G} \cdot \mathbf{S}_{\text{DBa}} \frac{e^{-jkr_i^{\text{DBa}}}}{r_i^{\text{DBa}}} \mathbf{E}_i \quad (2)$$

$$\mathbf{E}_s^{\text{DBb}} = \frac{e^{-jkr_s^{\text{DBb}}}}{r_s^{\text{DBb}}} \mathbf{S}_{\text{DBb}} \cdot \mathbf{G} \frac{e^{-jkr_i^{\text{DBb}}}}{r_i^{\text{DBb}}} \mathbf{E}_i \quad (3)$$

$$\mathbf{E}_s^{\text{TB}} = \frac{e^{-jkr_s^{\text{TB}}}}{r_s^{\text{TB}}} \mathbf{G} \cdot \mathbf{S}_{\text{TB}} \cdot \mathbf{G} \frac{e^{-jkr_i^{\text{TB}}}}{r_i^{\text{TB}}} \mathbf{E}_i \quad (4)$$

where \mathbf{E}_i is the Jones vector of the incident electric field expressed in the antenna polarization basis with its vertical $\hat{\mathbf{v}}$ and horizontal $\hat{\mathbf{h}}$ polarization components. \mathbf{E}_s^{xx} is the scattered Jones vector for the mechanism xx , \mathbf{S}_{xx} the 2 by 2 full-polarization complex scattering matrix (Sinclair matrix) for each mechanism, and \mathbf{G} the 2 by 2 Fresnel reflection matrix of the ground. The exponential terms model the propagation phase along the optical path of length r for each mechanism for the incident wave (suffix i) and the scattered wave (suffix s). k is the wave number in the air. This notation is for a spherical wave, but if the antennas are far enough from the scene, the property of local plane waves can hold. Finally, the radar signal is the coherent sum of each contribution of each mechanism:

$$\mathbf{E}_s = \mathbf{E}_s^{\text{SB}} + \mathbf{E}_s^{\text{DBa}} + \mathbf{E}_s^{\text{DBb}} + \mathbf{E}_s^{\text{TB}} \quad (5)$$

This mathematical formulation is used to simulate measurements with the ‘‘approximate’’ cylinder scattering model. For the convenience in this paper, the ground reflection matrix \mathbf{G} is diagonal (flat ground), and its coefficients are taken to be $G_{\text{vv}} = 1$ and $G_{\text{hh}} = -1$ for $\hat{\mathbf{v}}$ and $\hat{\mathbf{h}}$ polarizations as the ground is considered as a metallic surface.

2.3. The Direct Problem Formulation

To go further and better describe the modeling of measurements collected at a set of sensor positions and frequencies, we consider now the Single Bounce mechanism only (Equation (1)). Derivations for other scattering mechanisms will follow the same steps.

For the general case where emitting and receiving antennas have their own polarization basis ($\hat{\mathbf{v}}_i, \hat{\mathbf{h}}_i$) and ($\hat{\mathbf{v}}_s, \hat{\mathbf{h}}_s$), respectively, where $\hat{\mathbf{v}}$ and $\hat{\mathbf{h}}$ stand for vertical and horizontal polarizations, Equation (1) is fully described by explicit form:

$$\begin{pmatrix} E_{v_s} \\ E_{h_s} \end{pmatrix} = \frac{e^{-jk(r_s+r_i)}}{r_s r_i} \begin{pmatrix} S_{v_s v_i} & S_{v_s h_i} \\ S_{h_s v_i} & S_{h_s h_i} \end{pmatrix} \begin{pmatrix} E_{v_i} \\ E_{h_i} \end{pmatrix} \quad (6)$$

For a single polarization channel Equation (6) is reduced to the scalar expression:

$$E_s = \frac{e^{-jk(r_s+r_i)}}{r_s r_i} S E_i \quad (7)$$

where E_s and E_i can be either vertically or horizontally polarized, and S is the corresponding polarization complex scattering coefficient. It means that each polarization channel can be treated separately.

Notice that:

- as the transmitting and receiving antennas are located at a large distance from the scatterers compared to the region of interest, the electromagnetic wave is assumed to be a plane wave to compute the S coefficient whereas it is considered spherical from the wave path point of view to minimize locations approximations.
- the phase origin of the incident field is chosen to be on the emitting antenna, and its magnitude is normalized to 1, such as $E_i = 1e^{j0} \text{V} \cdot \text{m}^{-1}$. The study is then performed for a unitary incident field which can be removed from Equation (7) for readability reason, though still physically present.

By stacking the expression of Equation (7) for a set of M measurements distinguished by the pairs of incoming and outgoing directions and frequencies, and assuming that S does not depend on these parameters (like a “bright point”), the vector of measurements can be decomposed as a linear expression:

$$\begin{pmatrix} E_s^1 \\ \vdots \\ E_s^M \end{pmatrix} = \begin{pmatrix} \frac{e^{-jk_1(r_s^1+r_i^1)}}{r_s^1 r_i^1} \\ \vdots \\ \frac{e^{-jk_M(r_s^M+r_i^M)}}{r_s^M r_i^M} \end{pmatrix} \mathbf{S} = \mathbf{a}\mathbf{S} \quad (8)$$

Nevertheless for realistic scatterers, the coefficient S modeling the target is not constant according to the antennas parameters: frequency, incidence, and scattering directions. For given radar parameters and target properties, S becomes a vector whose values vary from a measurement configuration to another. Doing so, it characterizes the target’s electromagnetic signature. The vector of measurement \mathbf{E}_s has thus to be decomposed as the componentwise product of $\mathbf{a}(\mathbf{p})$, dependent on the relative target/antennas location \mathbf{p} , and $\mathbf{S}(\boldsymbol{\xi})$, dependent of the target properties set $\boldsymbol{\xi}$, which gathers the variables sought. Equation (8) is rewritten as:

$$\mathbf{E}_s(\mathbf{p}, \boldsymbol{\xi}) = \mathbf{a}(\mathbf{p}) \odot \mathbf{S}(\boldsymbol{\xi}) \quad (9)$$

where \odot symbolizes a term by term vector product making Equation (9) nonlinear.

3. THE INVERSE PROBLEM FORMULATION

3.1. Step 1: Direct Problem Linearization

With fixed target location and parameters, \mathbf{E}_s depends linearly on \mathbf{E}_i (Equation (7)). However, dependency on the location and parameters of the target is highly nonlinear. Before to be able to inverse the direct problem, it has first to be linearized.

To simplify the problem, we propose to approximate the set of possible vectors $\mathbf{S}(\boldsymbol{\xi})$ for a given range of parameters $\boldsymbol{\xi}$ by a linear subspace of dimension K , described by an orthonormal basis $\mathbf{U} = (\mathbf{u}_1, \dots, \mathbf{u}_K)$. \mathbf{E}_s in Equation (9) can then be approximated by

$$\mathbf{E}_s(\mathbf{p}, \boldsymbol{\xi}) \approx \mathbf{a}(\mathbf{p}) \odot \left(\sum_{k=1}^K X_k \mathbf{u}_k \right) \quad (10)$$

where X_k are the coefficients of the approximation of $\mathbf{S}(\boldsymbol{\xi})$ in the basis \mathbf{U} .

In order to determine the linear space used to approximate the model \mathbf{S} , prior information about the target is introduced. Ranges of parameters are fixed (radius a , height h , Euler tilt angles (α, β) , and complex relative permittivity ϵ_r), and a training set of vectors \mathbf{S} is computed using numerical simulations of the direct problem with the electromagnetic model (see 2.1). As the dependency on the position and \mathbf{S} are separable, the cylinder phase center is arbitrarily located at the (0,0,0) coordinates. A model order K is fixed, and the basis vectors $(\mathbf{u}_1, \dots, \mathbf{u}_K)$ are then obtained by computing the left singular vectors decomposition of the matrix collecting the training \mathbf{S} vectors.

When N multiple sources are present, the noisy measured field is decomposed as the sum

$$\mathbf{E}_s = \sum_{n=1}^N \sum_{k=1}^K (\mathbf{a}(\mathbf{p}_n) \odot \mathbf{u}_k) X_{nk} + \mathbf{r}_K + \mathbf{n} \quad (11)$$

where \mathbf{p}_n is the location \mathbf{p} of the n -th source, \mathbf{r}_K the approximation error vector, dependent on the position and parameters, and \mathbf{n} a measurement noise vector, which we will assume to be white, Gaussian, and independent on the target parameters. The problem is simplified by the linearization of the dependency of the model with respect to the target parameters. This simplification comes at the cost of a model error \mathbf{r}_K and a larger number of linear parameters X_{nk} , compared to the original nonlinear parameters.

3.2. Step 2: Location Estimation Using Group Sparsity

Equation (11) is the direct electromagnetic model for several cylinders centered at given locations.

To estimate the locations of the targets, we propose to use sparse estimation methods. A grid of possible locations is built $\mathbf{\Pi} = (\mathbf{z}_1, \dots, \mathbf{z}_P)$, and the measured field (11) can be assumed to be a sparse sum of sources located on the grid (that is, only a few sources have a nonzero contribution in the measured data):

$$\mathbf{E}_s = \sum_{p=1}^P \sum_{k=1}^K (\mathbf{a}(\mathbf{z}_p) \odot \mathbf{u}_k) X_{pk} + \mathbf{r}_K + \mathbf{n} \quad (12)$$

$$= \sum_{p=1}^P \mathbf{A}_p \mathbf{X}_p + \mathbf{r}_K + \mathbf{n} \quad (13)$$

where the matrix \mathbf{A}_p contains the vectors $\mathbf{a}(\mathbf{z}_p) \odot \mathbf{u}_k$ as columns, and the vector \mathbf{X}_p contains the coefficients of the source located at \mathbf{z}_p . It is assumed that most of the \mathbf{X}_p are zero. With \mathbf{A} obtained by horizontally concatenating the matrix \mathbf{A}_p , and \mathbf{X} the vertical concatenation of the \mathbf{X}_p , we obtain a simple linear model:

$$\mathbf{E}_s = \mathbf{A}\mathbf{X} + \mathbf{r}_K + \mathbf{n} \quad (14)$$

3.2.1. Problem Generalization: Scattering Mechanisms

We recall that the dictionary matrix \mathbf{A} has been obtained for a single interaction mechanism, the single bounce in Equation (6), and has to be renamed \mathbf{A}_{SB} . The process is the same to build the \mathbf{A}_{DBa} , \mathbf{A}_{DBb} , and \mathbf{A}_{TR} matrices for the double and triple bounce mechanisms. All the four are made with their respective target subspaces matrices \mathbf{U}_{SB} , \mathbf{U}_{DBa} , \mathbf{U}_{DBb} , and \mathbf{U}_{TR} . The global dictionary matrix is then the concatenation of the four mechanisms dictionary matrices such as:

$$\mathbf{A} = [\mathbf{A}_{\text{SB}}, \mathbf{A}_{\text{DBa}}, \mathbf{A}_{\text{DBb}}, \mathbf{A}_{\text{TR}}] \quad (15)$$

3.2.2. Group-Sparsity Constraint

The source localization problem relies on an imaging zone materialized by a 3D grid where each different cylinder is supposed to be located on a different node. That is the meaning of Equation (13). If the number of nodes is large enough compared to the cylinders number, which is easily achieved in forest radar imagery particularly at low frequencies, group sparsity property can be used conveniently. Compared to sparsity, where a vector is assumed to have a few nonzero coefficients, group-sparse vectors are assumed to be divided in blocks, and most of these blocks contain only zero coefficients. However, in non-zero blocks, the number of nonzero coefficients is not considered. Here, a block corresponds to a possible source location, and a nonzero block to a source is actually present in the domain. Each coefficient in a block corresponds to the weight of the vector \mathbf{u}_k in the approximation of the source scattering coefficient. In this block-OMP algorithm, as for a conventional OMP, sources are identified iteratively, by maximizing the energy of the projection of the data in the space corresponding to a source what we call, in this paper, the OMP criterion defined by:

$$\rho_{\mathbf{z}}(\mathbf{E}) = \|\mathbf{P}_{\mathbf{z}}(\mathbf{E})\|_2^2 \quad (16)$$

where \mathbf{E} is the data, and $\mathbf{P}_{\mathbf{z}}$ is the orthogonal projector on the space spanned by the K vectors $\mathbf{a}(\mathbf{z}) \odot \mathbf{u}_k$.

From the Block-OMP solution \mathbf{X} of Equation (14), a 3D image $\mathbf{I}(\mathbf{z}_p)$ is built for each mesh \mathbf{z}_p with:

$$\mathbf{I}(\mathbf{z}_p) = \sum_{k=1}^{K_{\text{supp}}} |X_k^{\mathbf{z}_p}|^2 \quad (17)$$

where K_{supp} is the sum of the subspace sizes K (in Equation (11)) for each scattering mechanisms.

3.3. Step 3: Scattering Pattern Reconstruction

Once the cylinders have been localized by their indices on the 3D meshing, their amplitudes can be estimated by solving the least-squares problem

$$\hat{\mathbf{X}}_{\text{scatt}} = \operatorname{argmin}_{\mathbf{X}} \|\mathbf{Y} - \mathbf{A}_{\text{scatt}} \mathbf{X}_{\text{scatt}}\|_2^2 \quad (18)$$

where $\mathbf{A}_{\text{scatt}}$ is the dictionary matrix \mathbf{A} non-orthonormalized but reduced by keeping only the columns corresponding to the nodes where the targets have been located. This additional step allows to use a scattering dedicated subspace size $K_{\text{scatt}} \neq K_{\text{supp}}$ whose effect is investigated in Section 4.4.

From Equations (9) and (10) it comes:

$$\mathbf{S}(\boldsymbol{\xi}) \approx \mathbf{U} \cdot \mathbf{X}_{\text{scatt}} \quad (19)$$

allowing the reconstruction of the \mathbf{S} values varying according to antennas parameters. That is, the radar signature of each target separately, for each scattering mechanism separately, is obtained depending on which block of $\mathbf{X}_{\text{scatt}}$ is chosen and using the corresponding \mathbf{U} .

3.4. Step 4: Biophysical Parameters Inversion

Inherently the direct “approximate” scattering model (see Section 2.1) computes the \mathbf{S}_{SB} , \mathbf{S}_{DBa} , \mathbf{S}_{DBb} , \mathbf{S}_{TB} terms of Equations (1) to (4) for a single cylinder whose phase center is located at the center of the system of axes. And the cylinder is described by its biophysical parameters (radius, height, tilt Euler angles, and complex relative permittivity). Therefore “approximate” model can be used to compute and minimize a cost function in an iterative inverse algorithm. To do so, we have chosen a Particle Swarm Optimisation (PSO) algorithm [25]. In this work, the swarm is composed of a population of 50 particles. We only use the estimated \mathbf{S}_{SB} term to compute a cost function as Equation (1) does not involve ground specular reflection \mathbf{G} coefficients (see 3.3). We compute the cost value for each particle, for a single polarization channel VV and for the M measurement configurations as:

$$\text{cost}^{\text{part.}} = \frac{1}{M} \sum_M \left(\left| \frac{\mathbf{S}_{\text{SB}} - \mathbf{S}_{\text{SB}}^{\text{part.}}}{\mathbf{S}_{\text{SB}} + \mathbf{S}_{\text{SB}}^{\text{part.}}} \right| \right) \quad (20)$$

where \mathbf{S}_{SB} is the column vector coming from Equation (19) associated with the scatterer under interest. It is the data set to fit with $\mathbf{S}_{\text{SB}}^{\text{part.}}$ which is the scattering coefficients vector computed for only one particle bio-physical parameters set. Each particle has its own cost value, and we assume that the particle with the lowest cost value provides the best biophysical parameters solution. The convergence criterion used here tests the stability of the biophysical parameters set obtained for the lowest cost particle during a fixed number of iterations. To validate the convergence, each PSO inversion has been further performed five times.

4. PRELIMINARY ASCERTAINMENTS

This section presents several aspects of the inversion model, for a single vertical cylinder lying on a metallic flat ground and then for both vertical and tilted cylinders. We show the key role of an imaging zone translation on CRBs and 3D image focalization. We investigate some properties of target subspaces to solve sources tilt angle estimation. Then we study the impact of the target subspaces sizes on the cylinder location and on the scattering coefficients inversion.

But we need first to introduce the Cramér-Rao Bounds (CRB) which are used to assess the results in noisy conditions.

4.1. CRB Generalities

The CRB is a lower bound on the variance of any unbiased estimator. These bounds can be used to design an experimental measurement setup, or assess the efficiency of an estimator. If the variance of an unbiased estimator reaches the CRB, the estimator is said to be a minimum-variance unbiased estimator (MVUE).

In general, CRBs are obtained under regularity conditions on the likelihood of the model and through the computation of the Fisher Information Matrix \mathbf{F} .

The covariance matrix of an unbiased estimator of a vector of parameters $\boldsymbol{\theta}$ is bounded by the inverse of the FIM:

$$E \left\{ \left(\boldsymbol{\theta} - \hat{\boldsymbol{\theta}} \right) \left(\boldsymbol{\theta} - \hat{\boldsymbol{\theta}} \right)^T \right\} \geq \mathbf{C}(\boldsymbol{\theta}) = \mathbf{F}^{-1} \quad (21)$$

In the case of a Gaussian model, where the measurements are assumed to be drawn according to

$$\mathbf{m} \sim \mathcal{N}(\mu(\boldsymbol{\theta}), \sigma^2 I) \quad (22)$$

the coefficients of the FIM are given by

$$\mathbf{F}_{ij}(\boldsymbol{\theta}) = \frac{1}{\sigma_m^2} \Re \left[\left(\frac{\partial \mu(\boldsymbol{\theta})}{\partial \theta_j} \right) \left(\frac{\partial \mu(\boldsymbol{\theta})}{\partial \theta_j} \right)^T \right] \quad (23)$$

In our application, the vector of parameters to be estimated is $\boldsymbol{\theta} = (\mathbf{p}, \boldsymbol{\xi})$, and the measurements \mathbf{E}_s , the VV-polarized scattered field, are given by Equation (5). Its derivatives are computed for a single representative scatterer whose each parameter is the mean value over its own seeking domain, except for the cylinder phase center height located at $x = y = 0$ and $z = \langle h \rangle / 2$. The unknown parameter vector $\boldsymbol{\theta}$ will be:

$$\boldsymbol{\theta} = [x, y, z, a, h, \Re(\epsilon_r), \Im(\epsilon_r)]^T \quad (24)$$

where x, y, z is the location of its phase center; a, h , and ϵ_r are respectively the radius and height of the cylinder and its relative permittivity.

Then, the diagonal terms of the CRB matrix yield lower bounds on the variance of the estimation of the parameters. The CRB associated with a parameter is homogeneous to a variance, and its dimension is the dimension of the parameter squared. In the next section, they will be compared to the covariances of the estimated parameters using the proposed methods, obtained by Monte-Carlo simulations.

4.2. Prerequisites on Antennas/Target Relative Locations

Antennas locations are defined separately on an upper half-sphere (z coordinate > 0) with the (R_i, θ_i, ϕ_i) spherical coordinates for each emitter and with (R_s, θ_s, ϕ_s) for each receiving antenna. That allows monostatic and bistatic configurations in the antennas coordinates frame. The imaging zone can be centered on the antennas coordinates frame or be translated according to the x and/or y axes. We present here the results of such translations that point out our choice to translate the center of the imaging zone. That will be illustrated by two kinds of results, CRB values and source localization.

4.2.1. The Effect of Scene Translation on CRBs

The CRB matrix, computed through Equations (23) and (21), is calculated for several xy -cylinder locations in order to investigate the effect of geometric symmetries between the cylinder location and the half-sphere supporting the antennas.

We have then computed the CRB matrix with $\sigma_m = \frac{P_{\text{signal}}}{\text{SNR}}$ for SNR = 20 dB and with a signal mean power $P_{\text{signal}} = \langle |\mathbf{E}_s|^2 \rangle_M$ with M being the measurements vector size. Locations on x and y axes have been chosen between -1500 m and $+1500$ m with steps of 100 m. The diagonal terms provide the covariance of each one of the seven parameters in $\boldsymbol{\theta}$ (Equation (24)). Here we have chosen to show the CRBs results in $[\text{m}^2]$ only for the radius a [m] and the cylinder phase center height z [m] in the z direction, as they are representative of the others.

Figures 2(a) and 2(b) show different range values but a complementary behaviour of the CRB(x, y) values respectively for the z location and a , particularly visible at the location $(x = 0, y = 0)$. CRB $_z$ coefficient is maximum whereas CRB $_a$ coefficient is minimum. Notice that CRB $_h$ and CRB $_z$ share the same behaviour, the highest levels at $(x = 0, y = 0)$, and CRB $_a, \text{CRB}_x, \text{CRB}_y, \text{CRB}_{\Re(\epsilon_r)}, \text{CRB}_{\Im(\epsilon_r)}$ too and the lowest levels at $(x = 0, y = 0)$.

CRB(x, y) boundaries values for each parameter are given in Table 1. We point out that CRB coefficients are conversely proportional to SNR. Numerical values of Table 1 can be used to get an order of magnitude for different SNR values.

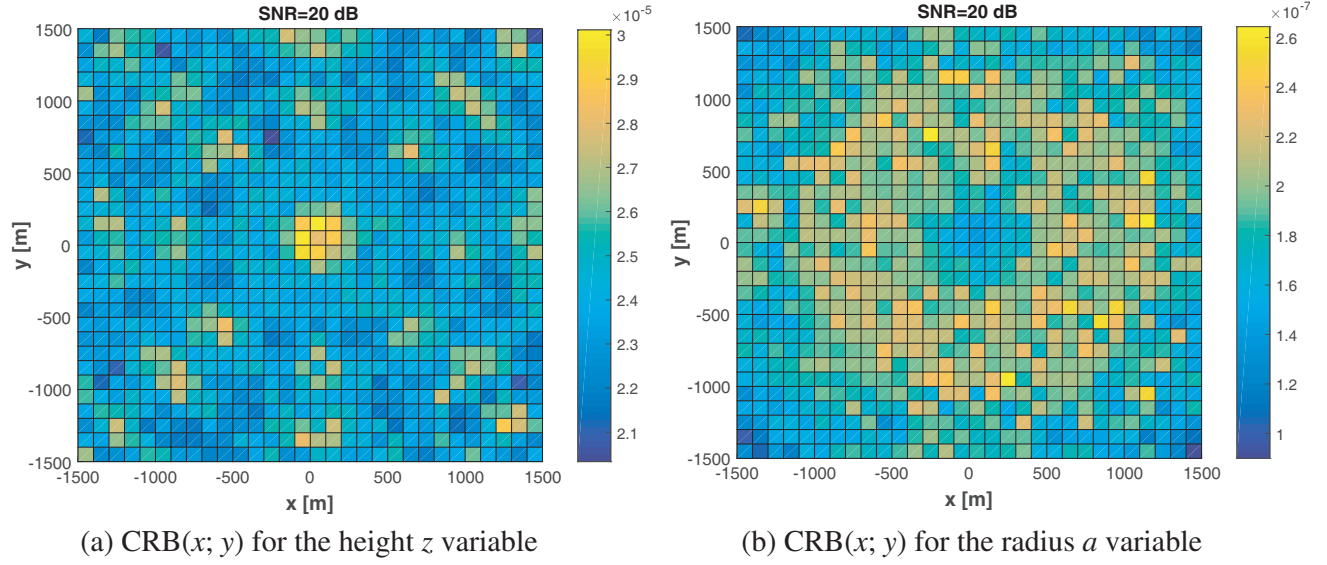


Figure 2. CRB(x, y) [m²] for (a) the height z and (b) the radius a variables with a maximum (resp. minimum) near $(x = 0, y = 0)$ in yellow (resp. blue).

Table 1. CRB(x, y) coefficients boundaries values with SNR = 20 dB.

CRB of parameter:	CRB(x, y) min value	CRB(x, y) max value
radius a [m ²]	8.9e-08	2.6e-07
height h [m ²]	7.8e-05	1.3e-04
x -phase center location [m ²]	2.1e-07	7.1e-07
y -phase center location [m ²]	2.1e-07	6.5e-07
z -phase center location [m ²]	2.0e-05	3.0e-05
Permittivity real part $\Re(\epsilon_r)$	1.3e-02	2.8e-02
Permittivity imaginary part $\Im(\epsilon_r)$	3.9e-03	1.2e-02

Lowering the CRB coefficients using the cylinder xy -location and by extension, the xy -location of the imaging zone has no best global solution. But if we aim to inverse the xyz -location of a cylinder as precisely as possible particularly in z , we would have to choose an imaging zone center far away from the global coordinate center.

4.2.2. The Effect of Scene Translation on 3D Imaging

The example shown in this section aims to highlight the effect of scene translation on the OMP process itself. That is why the problem $\mathbf{E}_s = \mathbf{A}\mathbf{X} + \mathbf{r}_K$ is solved (Equation (14)) without noise. A single vertical cylinder is placed upon a metallic ground and is measured in VV polarization. The \mathbf{A} matrix is given by the Equation (15).

We investigate the consequences of the imaging zone translation on the OMP process by comparing two configurations, with the imaging zone being translated or not: $\mathbf{C}_{loc} = [-1000, 1000, 0]$ m or $\mathbf{C}_{loc} = [0, 0, 0]$ m where \mathbf{C}_{loc} is the center of a local coordinate system used to locate the cylinder in the imaging zone. Therefore, it is also a vector depicting the translation of the imaging zone center from the antennas coordinates center. As a result, Figure 3 shows the spread of $\rho(\mathbf{z})$ (Equation (16)) in 1-dimension according to the z -axis direction for the cylinder (x, y) true location.

This numerical experiment shows:

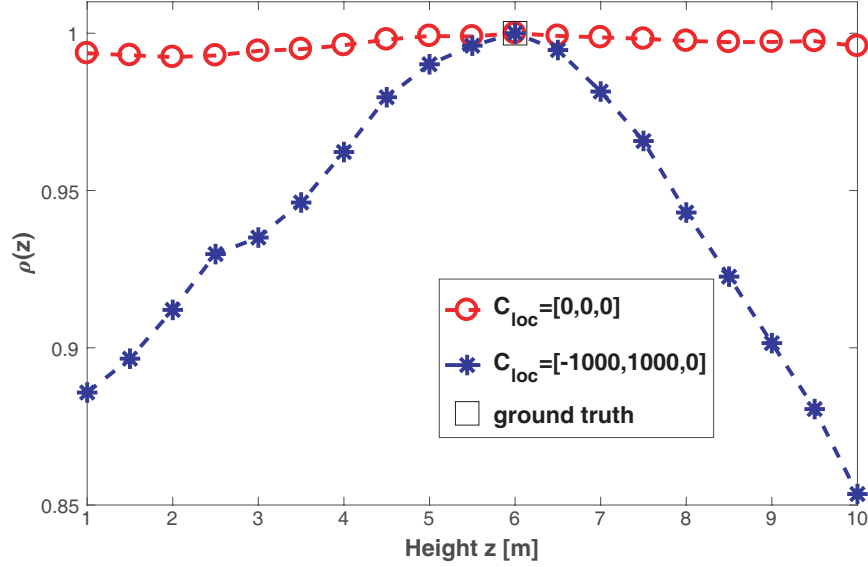


Figure 3. Normalized $\rho(z)$ (Equation (16)) according to height z (m) at the (x, y) ground truth location for $\mathbf{C}_{loc} = [0, 0, 0]$ m and $\mathbf{C}_{loc} = [-1000, 1000, 0]$ m.

- The subspace decomposition works efficiently by giving the maximum power of Equation (17) at the ground truth height location (the cylinder phase center is at 6 m height depicted by the black square) whatever the translation is.
- The $\mathbf{C}_{loc} = [-1000, 1000, 0]$ m translation clearly enhances the image focalization in z axis direction what could be useful to enhance the resolution.

This example explains why, even if the source location is successful in both cases, we have chosen to translate the imaging zone to avoid locations errors in the case of two tree branches located one above the other.

More generally, this example points out the effect of the antennas-imaging zone relative locations on image focalization and asks clearly the question of optimizing the antennas carrier trajectory.

4.3. 3D Imaging: Subspaces Properties according to Cylinder Tilt Angle

A single target subspace allows decompositions for cylinders of different sizes and different permittivities on parameters ranges large enough for an application to tree trunks or large primary branches (see Section A.2). But subspace decomposition is more sensitive to tilt angles range, and it would be interesting to take advantage of this property. Here we show the example of two cylinders differing by their size, permittivity, and tilt angles. Two different subspaces are built, and the two databases (see Section 3.1) differ only by the tilt angle used to compute them: one typical cylinder is vertical, and the other is tilted by $\alpha = 30^\circ$ and $\beta = 60^\circ$ Euler angles (see Section A.1.1).

OMP results are shown as 3D images $I(\mathbf{z}_p)$ (Equation (17)) in Figure 4 under additive Gaussian noise constraint (SNR = 20 dB and $N_{test} = 1000$ noisy vector measurement samples). The 3D imaging zone range is $[\min = -2.5 \text{ m}, \max = 2.5 \text{ m}]$ on x and y axes, and $[\min = 1 \text{ m}, \max = 10 \text{ m}]$ on z axis, by steps of 0.5 m. It is translated from the antennas origin with a $\mathbf{C}_{loc} = [-1000, 1000, 0]$ m vector. In the 3D imaging zone local coordinates, the cylinders phase centers are located at $[1.5, -1, 6]$ m and $[-1, 2, 5]$ m for the vertical and the tilted cylinders, respectively.

Four cases are presented here. The first one (Figure 4(a)) shows that the vertical cylinder measurements which have been projected on a target subspace (TSS) computed for a vertical cylinder provide a correct location. Figure 4(b) points out an important result: when a tilted cylinder is projected on a target subspace which has been computed for a vertical typical cylinder, 3D imaging fails for each one of the N_{test} OMP runs. To obtain an accurate estimation of the position, the tilted cylinder measurements have to be projected on a target subspace built with the appropriate tilted typical target

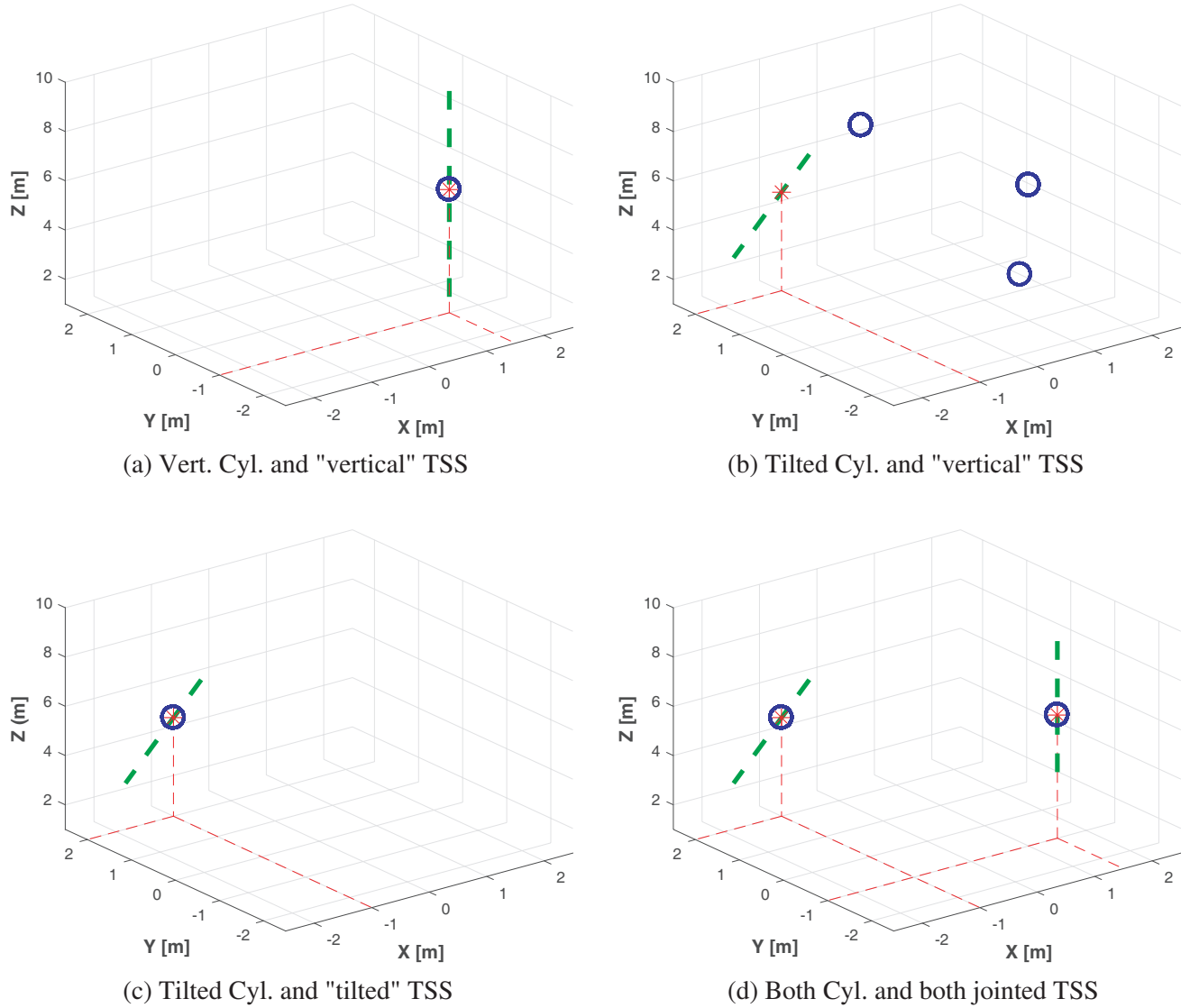


Figure 4. OMP 3D images $I(\mathbf{z}_p)$ for (a), (b), (c) one and (d) two cylinders: vertical and/or tilted cylinder projected on a “vertical” and/or “titlted” Target SubSpace (TSS) obtained for $N_{test} = 1000$ noisy measurement samples ($SNR = 20$ dB). Red star: cylinder phase center ground-truth location. Red dashed lines: location projection on coordinate axis. Bold Green dashed lines illustrate each cylinder axis. Blue circle: superposition of the N_{test} OMP solutions.

(Figure 4(c)). Here, this tilt angle has been chosen equal to the ground truth ($\alpha = 30^\circ$ and $\beta = 60^\circ$) to illustrate that introducing *a priori* information on tilt angles through the target subspaces is necessary to localize accurately target echoes. Finally, Figure 4(d) shows the solution of the 3D imaging process for both tilted and vertical cylinders together by using jointed vertical and tilted cylinder target subspaces. The OMP algorithm detects both targets at the true location for each noisy measurement vector sample.

Notice that the OMP algorithm provides the same solution for each noisy measurement sample. This means that it is not sensitive to an $SNR = 20$ dB weak noise level at this space meshing size of $[0.5, 0.5, 0.5]$ m. The effect of noise on the target location retrieval is investigated in Section 5.

Furthermore, the structure of the solution vector \mathbf{X} of Equation (14) provides more information. Indeed, it owns the same structure as the dictionary matrix \mathbf{A} (Equation (15)), by blocks of meshing, scattering mechanisms, and target subspaces. As an illustration of that, the OMP criterion $\rho_{\mathbf{z}}$ (Equation (16)) is plotted under additive gaussian noise conditions as histograms (for $N_{test} = 1000$

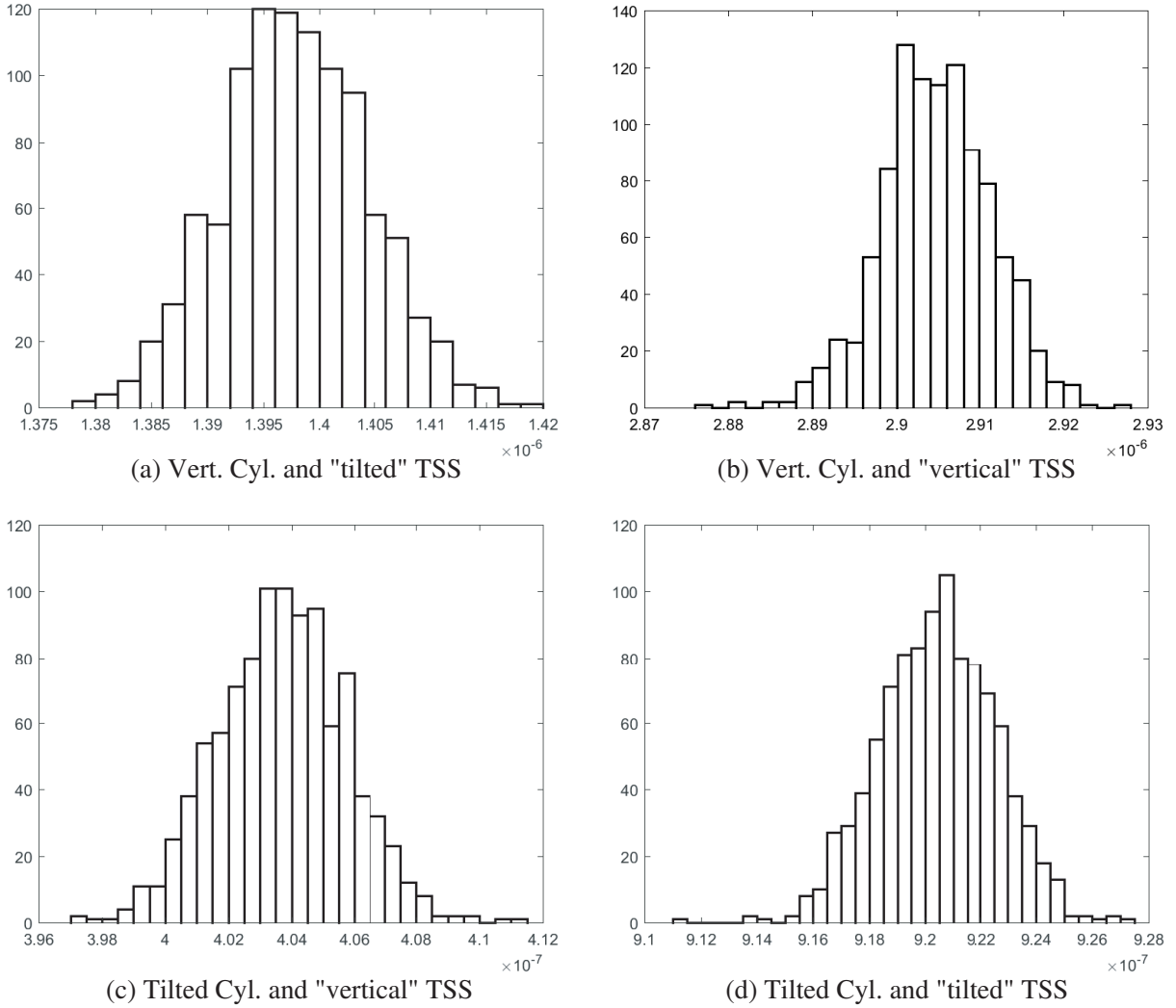


Figure 5. Histograms of the OMP criterion values ($\rho_{\mathbf{z}}$ in Equation (16)) computed with a “vertical” and a “tilted” Target SubSpace (TSS) for a vertical and a tilted cylinder and for $N_{test} = 1000$ noisy measurements vectors samples (SNR = 20 dB). Upper figures (a) and (b) for a vertical cylinder and lower figures (c) and (d) for a tilted cylinder. From left to right, increasing histograms abscisses values showing increasing values when the well-suited TSS is chosen, even in presence of noise.

noisy measurements vectors samples with SNR = 20 dB) in Figure 5. Two configurations are under test: the case of a vertical cylinder, upper figures (a) and (b), and the case of a tilted cylinder, lower figures (c) and (d). For both cylinder tilt configurations, Block-OMP algorithm has been processed using a vertical or a tilted Target SubSpace (TSS). It means that the orthogonal basis \mathbf{U} (see 3.1) is built from a typical vertical or tilted cylinder. Figure 5 shows clearly that a vertical cylinder measurement has a larger OMP criterion when the corresponding Target SubSpace is used even in the presence of noise.

The main conclusion is that in a realistic imaging process where we are looking for a cylinder with an unknown tilt angle, we would have to build several target subspaces for different tilt angles. Therefore, we would have to mesh the tilt angles ranges and consider each angle configuration as the center of a patch. Then all the patches would have to be merged to cover all the tilt angles range. This method has to be further investigated, but if it is practicable the main drawback would be the huge size of the dictionary matrix \mathbf{A} in Equation (15). On the other hand, the main advantage is that the information about each cylinder’s tilt angles is contained within the OMP outgoing vector \mathbf{X} .

4.4. Inversion Process: The Effect of the Subspace Size

In this section, we investigate the effect of the truncation order K on the SVD used to build the basis \mathbf{U} modeling the scattering coefficients for a range of physical parameters set ξ .

Bias and variance of the estimation of the location and the scattering coefficient in VV polarization are estimated by numerical simulations, with following parameters: a single vertical or tilted cylinder measurement is simulated according to $M=2000$ antennas parameters sets (see Section A.1.1). A SNR = 20 dB white Gaussian noise is added leading to $N_{test}=1000$ noisy measurement vector samples. The OMP algorithm is applied to solve the source localization problem for several subspaces dimensions K (Section 4.4.1). Then the VV scattering coefficient (Section 4.4.2) is computed from the least-squares solver (Equation (18)) followed by the change of basis (Equation (19)) using an increasing subspace size K .

For both location and scattering coefficient estimation, with increasing K , bias decreases. However, the degree of freedom increases with the subspace size K , and it is expected that the variance degrades. Then the Mean Square Error (MSE), sum of the variance and bias squares, presents a minimum. We note that this optimal K will depend on the noise level.

4.4.1. Source Localization

The dictionary matrix in Equation (15) is built for 14 sets of increasing subspaces sizes with $K_{supp} = K_{supp}^{SB} + K_{supp}^{DBa} + K_{supp}^{DBb} + K_{supp}^{TB}$ and for each scattering mechanism: $K_{supp}^{SB} = K_{supp}^{TB} = 2 + 3k$ and $K_{supp}^{DBa} = K_{supp}^{DBb} = 2 + 2k$ with $0 \leq k \leq 13$.

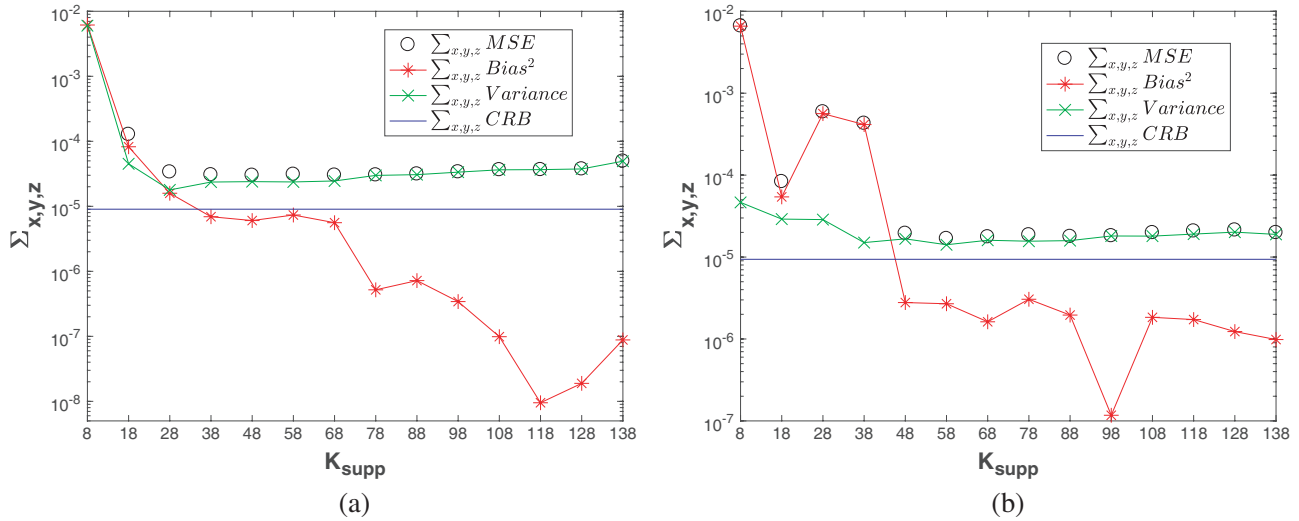


Figure 6. Location estimation MSE, Bias², Variance and CRB versus Target Subspace size configuration, K_{supp} . $N_{test} = 1000$ noisy measurement vector samples with SNR = 20 dB additive white gaussian noise. (a) Vertical cylinder. (b) Tilted cylinder.

Figure 6 indicates different shapes but similar MSE trends with an acceptable minimum for the sixth size configuration for both vertical (Figure 6(a)) and tilted (Figure 6(b)) cylinders. That is:

- Vertical cylinder: $[K_{supp}^{SB}, K_{supp}^{DBa}, K_{supp}^{DBb}, K_{supp}^{TB}] = [17, 12, 12, 17]$.
- Tilted cylinder: $[K_{supp}^{SB}, K_{supp}^{DBa}, K_{supp}^{DBb}, K_{supp}^{TB}] = [17, 12, 12, 17]$.

Notice that CRB remains always lower than the variance, as expected.

4.4.2. Scattering Coefficient

For the VV scattering coefficient estimation, the total subspaces size $K_{scatt} = K_{scatt}^{SB} + K_{scatt}^{DBa} + K_{scatt}^{DBb} + K_{scatt}^{TB}$, the four being equal and following $K_{scatt}^{SB} = 2 + 6k$ with $0 \leq k \leq 13$.

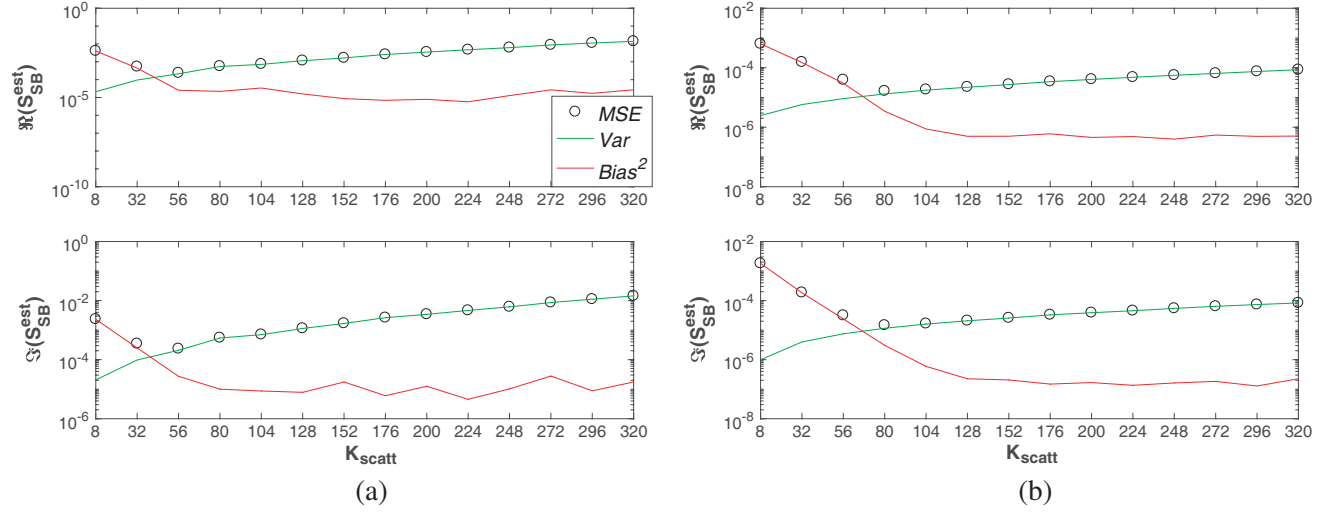


Figure 7. MSE, Bias², and Variance versus size subspaces configurations K_{scatt} of the estimated scattering coefficient S_{SB}^{est} . (a) Vertical cylinder. (b) Tilted cylinder.

Figure 7 shows only the MSE, the bias, and the variance for the single bounce mechanism as only this scattering mechanism is used for biophysical parameters retrieval (see Section 3.4), but the three other mechanisms provide similar results. For the vertical cylinder (Figure (a)), both real and imaginary parts of S_{SB}^{est} provide a lowest MSE for the third configuration whereas it is the fourth configuration for the tilted cylinder (Figure (b)). That is:

- Vertical cylinder: $[K_{scatt}^{SB}, K_{scatt}^{DBa}, K_{scatt}^{DBb}, K_{scatt}^{TB}] = [14, 14, 14, 14]$.
- Tilted cylinder: $[K_{scatt}^{SB}, K_{scatt}^{DBa}, K_{scatt}^{DBb}, K_{scatt}^{TB}] = [20, 20, 20, 20]$.

Notice that CRBs are not computed for the scattering coefficients but only for the biophysical parameters. Such comparisons are presented in Section 5.

5. INVERSION PROCESSING EXAMPLE

This section investigates the effect of noisy M measurements vector such as $\mathbf{E}_s = \mathbf{A} \cdot \mathbf{X} + \mathbf{n}$ where \mathbf{n} is an additive noise vector following the Gaussian normal law $\mathcal{N}(0, \sigma^2 \cdot \mathbf{I}_d)$. The variance σ^2 is obtained through an arbitrary Signal-to-Noise Ratio value such as $\text{SNR} = \langle |\mathbf{E}_s^{NO\ noise}|^2 \rangle_M / \sigma^2 = 20$ dB. Noisy simulations are performed over $N_{test} = 1000$ samples of noisy measurements \mathbf{E}_s vectors (see simulations parameters in Section A.1.1).

Antennas locations are illustrated in Figure 8(a). They are spread over a hemisphere according to linearly spaced incidence and azimuth angles. Antennas are either receivers or emitters allowing monostatic and bistatic configurations. Each antenna points at the imaging zone which is reduced to a point at this large scale, centered at $\mathbf{C}_{loc} = [-1000, 1000, 0]$ m coordinates.

In this example, we will further study the problem of two cylinders (see Figure 8(b)). In the previous Section 4.3, Figure 4(d) provided the OMP results of location estimation for N_{test} noisy measurements vectors. 3D image (Equation (17)) was given in the local coordinates system, with a \mathbf{C}_{loc} translation vector. This simulation has shown clearly that the inversion process is not sensitive to a noise power corresponding to a $\text{SNR} = 20$ dB at a large scale meshing, 0.5 m^3 cube as illustrated in Figure 8(b): the ground truth, N_{test} estimated locations, and their average are found at the same place. If we want to observe the effect of noise at lower scale, both cylinders have to be treated separately to achieve a meshes size small enough.

For each cylinder separately, $N_{test} = 1000$ noisy measurements vectors samples are simulated independently assuming an additive white Gaussian noise. The inversion process described in this

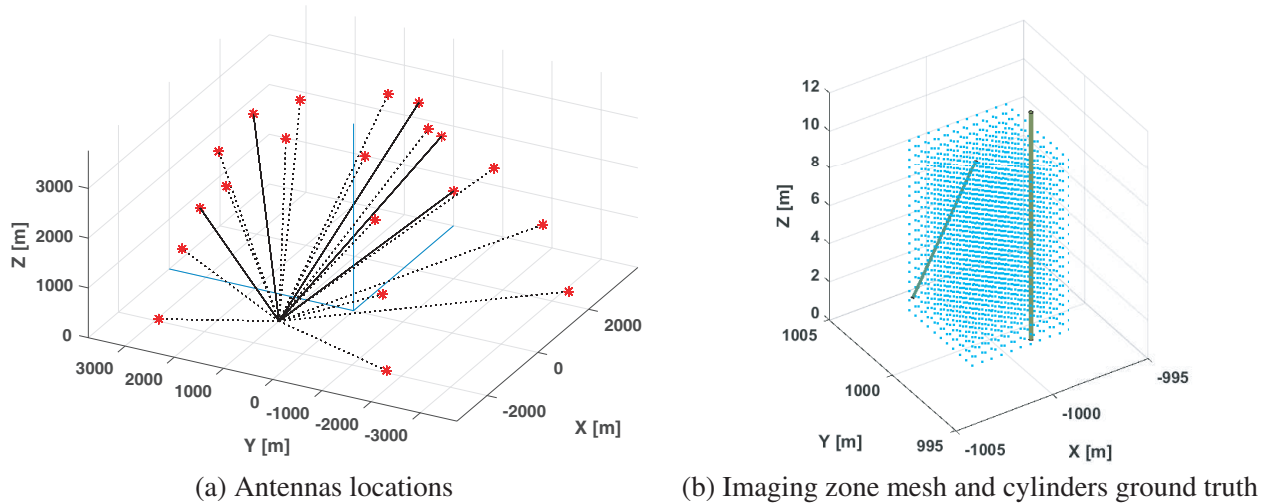


Figure 8. (a) Antennas locations in their coordinates system: Blue direct trihedral. Red star: emitters and receivers locations. Antennas are pointing toward the imaging zone (dotted lines) located according to the $\mathbf{C}_{loc} = [-1000, 1000, 0]$ m translation vector. (b) Mesh of the imaging zone (blue dots) with both cylinders. Notice that even if the cylinders overflow the mesh, their phase centers remain inside.

paper is repeated for each noisy measurement sample. The figures shown in this section (histograms and 3D images) are then the results of a Monte-Carlo approach.

5.1. Location Estimation

The source localization problem is solved N_{test} times by the OMP algorithm. Figure 9 provides the resulting 3D image whereas Figure 10 shows the same results as histograms for the (x, y, z) cylinder phase center coordinates, in meters. Notice the imbalance between the scales in z and x, y . The point cloud is clearly ellipsoid-shaped and its main axis oriented according to the cylinder lengthwise axis. A

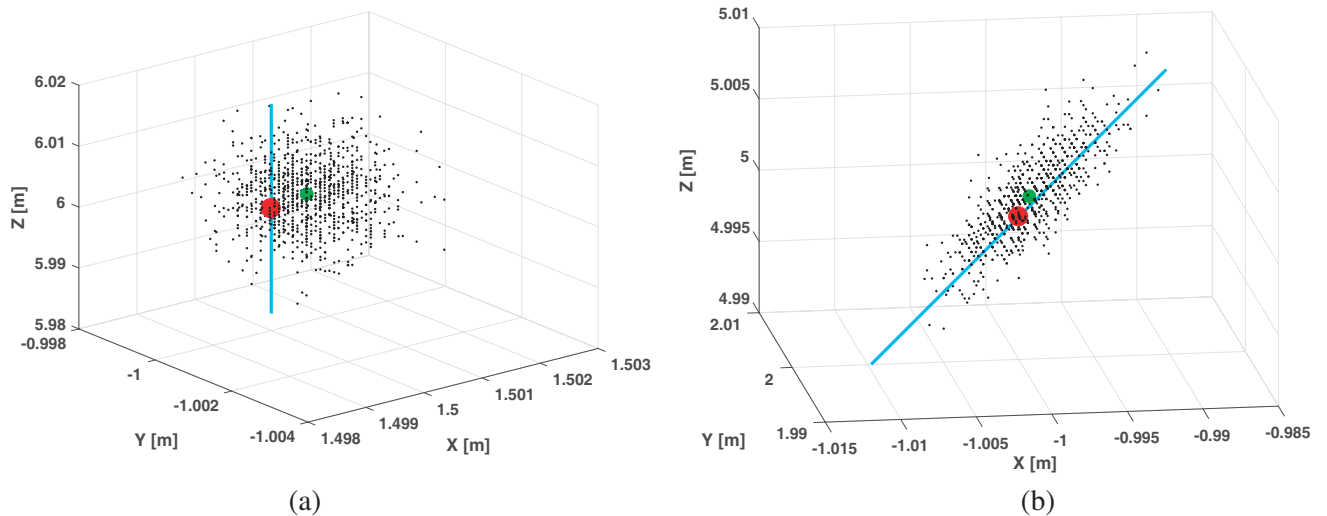


Figure 9. 3D image (Equation (17)) of OMP estimation of Cylinders locations (SNR = 20 dB and $N_{test} = 1000$ noisy measurements vectors samples) Black dots: N_{test} estimated locations. Cyan lines: cylinder axis ground truth. Red circles: ground truth phase center location. Green Circles: mean locations averaged over the N_{test} estimations. (a) Vertical cylinder. (b) Tilted cylinder.

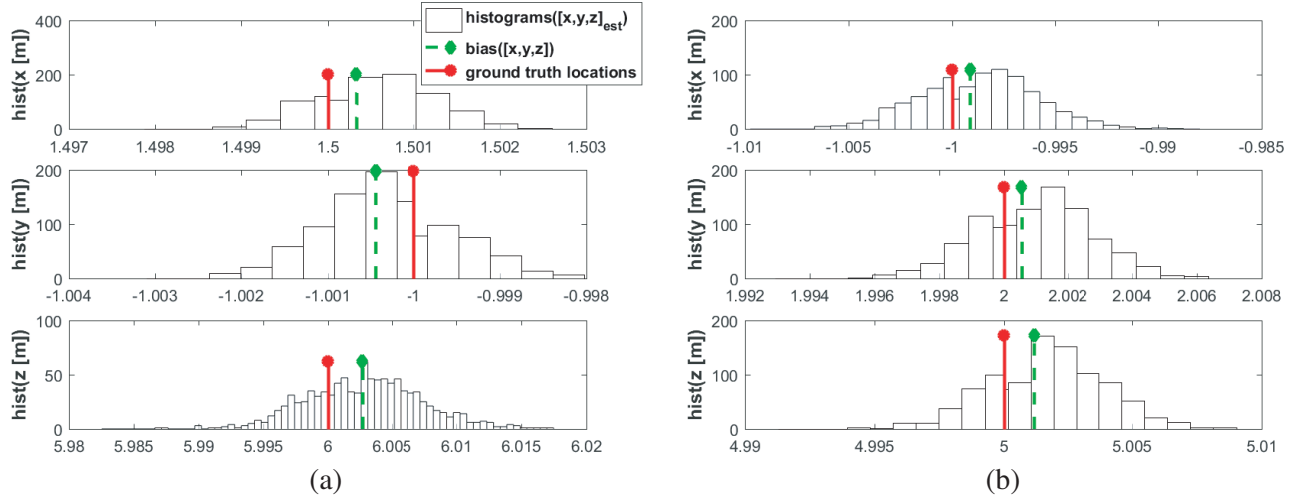


Figure 10. Histograms of cylinder estimated locations $[x, y, z]_{est}$ in [m] for SNR = 20 dB and $N_{test} = 1000$ noisy measurements vectors samples. (a) Vertical cylinder. (b) Tilted cylinder.

weak location bias of the order of a few millimeters appears as a consequence of the trade-off between the bias and the variance when subspaces sizes have been chosen (see Section 4.4.1). Nevertheless, tilted cylinder location estimation seems to be more accurate.

5.2. Biophysical Parameters Estimation

Figure 11 provides the results of the biophysical parameters estimation (radius a , height h and relative complex permittivity ϵ_r) as histograms, obtained through the PSO algorithm (see Section 3.4). As a global representative estimator, we decide to show the result of this procedure to obtain the magenta stems:

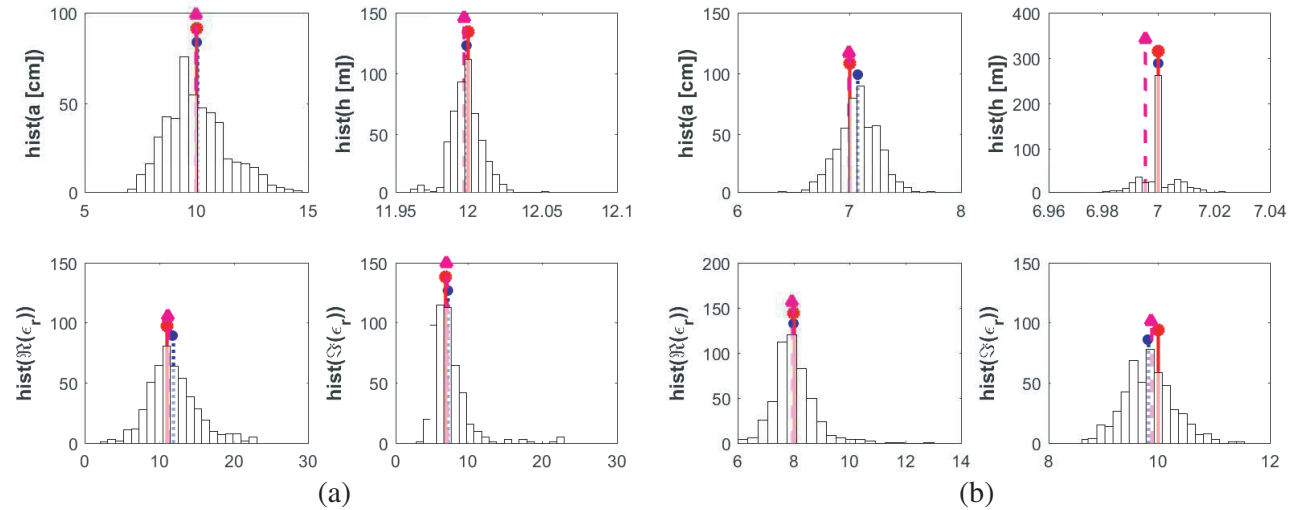


Figure 11. PSO estimation histogram $\text{PSO}(\mathbf{S}_{\text{SSB}}^{\text{est}})$ of the cylinder physical parameters: radius a [cm], height h [m] and real and imaginary parts of the relative permittivity ϵ_r . Red stem: parameter ground truth. Blue dotted stem: $\langle \text{PSO}(\mathbf{S}_{\text{SSB}}^{\text{est}}) \rangle_{N_{\text{test}}}$. Magenta dashed stem: $\text{PSO}(\mathbf{S}_{\text{SSB}}^{\text{est}} \leftarrow (\langle [x, y, z]_{est} \rangle_{N_{\text{test}}}, \langle Y_N \rangle_{N_{\text{test}}}))$. $N_{test} = 500$ for time consuming reasons. (a) Vertical cylinder. (b) Tilted cylinder.

- Choose the biased location of the previous location estimation, $\mathbf{bias}([x, y, z]_{est})$ (green results in Figures 9 or 10).
- Estimate the scattering coefficients for a target at this location from Equations (18), (19) and extract the single bounce contribution \mathbf{S}_{SB}^{est} .
- Perform a single PSO estimation for this \mathbf{S}_{SB}^{est} database.

Results are pretty good when comparing the parameters estimate to the corresponding mean parameter averaged over the $N_{test} = 500$ PSO estimations or to the ground truth. It is all the more important that the PSO process is particularly slow: we have been obliged to reduce the N_{test} value from 1000 to 500 to keep an acceptable computation time but far away from what is called real time. Reducing the process to a single PSO estimation is then a challenge.

5.3. Covariance and CRB Predictions

The last results presented in this paper are gathered in Table 2. Homogeneous to a standard deviation, they are the square root of the diagonal terms of the CRB and the covariance matrices, respectively $\sigma_{CRB} = \sqrt{CRB}$ and $\sigma_{cov} = \sqrt{\text{diag}(\text{covariance})}$. Notice that the covariance matrix is obtained using the $N_{test} = 500$ samples of the cylinder estimated parameters set $\xi_{est} = (\text{radius } a, \text{ height } h, \text{ phase center locations } (x, y, z), \text{ and relative permittivity } \epsilon_r)$. These results lead to the conclusions:

- σ_{CRB} coefficients are less than the covariance ones, to see as a numerical validation.
- (x, y, z) -locations values indicate that a minimum variance unbiased estimator (MVUE) is found as σ_{CRB} and σ_{cov} coefficients are in the same neighborhood. Furthermore, σ_{CRB} for z coordinate is larger than for (x, y) ones when being computed for a vertical cylinder, whereas for the tilted one, the σ_{CRB} for (x, y, z) coordinates is more balanced. One can observe here the effect of the cylinder's main axis tilt.
- as found before, σ_{CRB} coefficients for height and radius are a bit weaker for the tilted cylinder than for the vertical one. σ_{cov} coefficients are larger but have the same trend.
- σ_{cov} coefficients for ϵ_r are unacceptably huge, particularly for the vertical cylinder.

Comparisons between σ_{cov} and σ_{CRB} coefficients predict that a better estimator exists for biophysical parameters estimation than the PSO does. To reach a better estimation with a much lower variance is a crucial issue for the relative permittivity.

Table 2. Covariance and CRB of biophysical parameters for noisy simulated data.

Phys. parameter	Vertical Cylinder		Tilted Cylinder	
	σ_{CRB}	σ_{cov}	σ_{CRB}	σ_{cov}
radius a [m]	2.5e-4	1.4e-2	1.6e-4	1.8e-3
height h [m]	6.2e-3	1.05e-2	5.3e-3	6.1e-3
x location [m]	4.7e-4	6.6e-4	2.3e-3	2.7e-3
y location [m]	5.6e-4	7.4e-4	1.4e-3	1.7e-3
z location [m]	2.9e-3	4.6e-3	1.5e-3	2.2e-3
$\Re(\epsilon_r)$	8.9e-2	3.4	9.5e-2	7.5e-1
$\Im(\epsilon_r)$	4.4e-2	2.6	7.7e-2	4.5e-1

6. CONCLUSIONS AND DISCUSSION

This paper introduces an original way to inverse the physical parameters of two different dielectric cylinders lying above a PEC soil, seen as a “primitive” tree from an electromagnetic point of view, using VV-polarization low-frequencies (300–320 MHz) radar simulated data. Simulation results prove that a first step forward is taken successfully using:

- a target subspace decomposition based on simulations which is an efficient way to introduce *a priori* information and to linearize the physical problem allowing a full-inversion.
- a sparse optimization method which is particularly well suited for 3D imaging applications
- a block structure enabling to retrieve the scattering coefficient separately:
 - for each target (cylinder)
 - for each polarization channel (expected theoretically)
 - for each scattering mechanism
- a stochastic inversion algorithm to estimate the biophysical parameters.

Finally, this first study aims to identify what is necessary to process simulated data and to point out the relevant questions for further investigations, that are:

- Investigate other estimators for scattering complex coefficients and biophysical parameters retrieval.
- a direct scattering model is used to simulate pure and noisy radar measurements. Its formalism is also used to inspire the inversion process. That constitutes a typical “inverse crime” case. One way to overcome this lack would be to simulate measurements with another electromagnetic direct model such as [18] which has been validated in [19, 20].
- As we have built one target subspace for each cylinder orientation, one could imagine studying the ability of this inversion process to recognize targets types through their respective target subspace: target recognition application.
- How to sample physical parameters domain to build a relevant database for target subspaces?
- From a general point of view, we could imagine a large set of target subspaces computed for several tilt angles samples to image any tilted cylinder and extract a tilt angle information from the target subspaces. But one question arises: how to sample appropriately the tilt angles ranges and extract a tilt angle in this case?
- Introduce the spatial resolution minimization as a prior constraint.
- How to take into account a more realistic scattering model of the soil? A dielectric flat ground reflection coefficient \mathbf{G} in Equation (1) would introduce soil permittivity parameter. How does it impact the process? Would this process be able to retrieve soil parameters?

APPENDIX A. ALGORITHM INPUTS

A.1. Measurements Simulation Inputs

A.1.1. Ground Truth Parameters

First, we build a ground truth by defining the geometric dimensions of each cylinder (the radius a , the height h), its tilt if needed (the Euler angles α and β), its phase center coordinates (x, y, z) , and its complex relative permittivity ϵ_r . The soil is modelled as a perfect conducting plane. The parameters used to simulate a vertical and a tilted cylinder respectively are:

- radius $a = 10$ and 7 cm.
- height $h = 12$ and 7 m.
- location of the phase center in the imaging box mark $x = 1.5$ m, $y = -1$ m, $z = 6$ m ($= h/2$) and $x = -1$ m, $y = 2$ m, $z = 5$ m ($> h/2$).
- Euler tilt angles $\alpha = 0^\circ, \beta = 0^\circ, \gamma = 0^\circ$ and $\alpha = 30^\circ, \beta = 60^\circ, \gamma = 0^\circ$.
- cylinder relative permittivity $\epsilon_r = 11 - i.7$ and $\epsilon_r = 8 - i.10$. $(-)$ indicates a $\exp + i\omega t$ time convention.
- for simplification purpose the metallic ground is directly taken into account through its Fresnel reflection coefficients (1 for the VV polarization and -1 for the HH one, both gathered in a diagonal matrix reflection operator).

A.1.2. Antennas Parameters

Second, we define radar parameters with frequencies, polarizations of interest, and antennas locations. As we allow monostatic and bistatic configurations, antennas locations are defined separately for the emitter with the (R_i, θ_i, ϕ_i) spherical coordinates with (R_s, θ_s, ϕ_s) for the receiving antenna. Furthermore, we can apply an additive zero-centered gaussian noise through a signal to noise ratio (SNR) on the simulated radar measurements.

As a first step and for simplification purpose, we omit to take into account the antennas radiation pattern. That supposes a narrow primary lobe always directed toward the center of the target searching box (the imaging zone) whose location is depicted by the translation vector \mathbf{C}_{loc} in this paper.

The simulation parameters are:

- 5 linearly spaced frequencies in the range $freq = [300; 320]$ MHz.
- the radius of the half-sphere $R_s = R_i = 4000$ m.
- 4 linearly spaced zenithal angles in the range $[20; 80]^\circ$ for θ_s and θ_i and 5 azimuth angles respectively $[0; 4/5 * 360]^\circ$ for ϕ_s and ϕ_i .
- the total number of measurements used is then $M = 2000$.
- polarization of interest is VV even if the electromagnetic scattering models we developed can simulate the four polarization channels (co- and cross-pols).
- a SNR = 100 in linear scale or SNR = 20 dB and $N_{test} = 1000$ (or $N_{test} = 500$ for PSO computations) noisy measurement vectors samples.

A.2. Inversion Processing Inputs

The inversion process needs its own parameters. The dedicated inputs provide boundaries on the sought parameters.

A.2.1. Meshing Parameters

The volume of interest where we want to locate the target (a cylinder) is defined as a meshing in the three directions for 3D imaging. For each (x, y, z) dimension the user provides a minimum, a maximum, and a mesh size value. This 3D box can be translated according to the global coordinate axes with the $\mathbf{C}_{\text{loc}} = [\tau_x, \tau_y, \tau_z]$ vector. This allows breaking the geometrical symmetries between the antennas half-sphere locations and the imaging box meshes.

- the meshing on x axis: $[-2.5, 2.5, 0.5]$ m.
- the meshing on y axis: $[-2.5, 2.5, 0.5]$ m.
- the meshing on z axis: $[1, 10, 0.5]$ m.
- translation from the global axis center: $\mathbf{C}_{\text{loc}} = [0, 0, 0]$ m or $[-1000, 1000, 0]$ m.

A remark on the minimum value of the grid on z axis: it is not equal to zero because, for a mesh on the ground single, double and triple bounce scattering mechanisms are no more distinguishable by their propagation phases. Moreover, that configuration would mean that trunks or branches were horizontally lying on the ground and inside for a half.

A.2.2. Biophysical Parameters

Each cylinder parameter is bounded in a realistic domain. This domain and the values taken inside are used to build a target subspace (see 3.1). They are defined such as:

- the radius bounds $bound_a = 6$ to 12 cm with 7 linearly spaced samples.
- the height bounds $bound_h = 6$ to 14 m with 9 linearly spaced samples.
- the real part of the relative permittivity bounds $bound_{Repsr} = 6$ to 12 with 7 linearly spaced samples.
- the imaginary part of the relative permittivity bounds $bound_{Impsr} = 6$ to 12 with 7 linearly spaced samples.

A.2.3. Target Subspace Size

The inversion process involves the target subspace vectors (see Section 3.1): retrieving the target location (Section 3.2) and the scattering coefficient inversion (Section 3.3). There are different target subspaces for each scattering mechanisms (single, double and triple bounces). The size K of each of them is chosen according to the results obtained in Section 4.4: The target subspace size for target localization, namely the support:

- Vertical cylinder: $[K_{supp}^{SB}, K_{supp}^{DBa}, K_{supp}^{DBb}, K_{supp}^{TB}] = [17, 12, 12, 17]$.
- Tilted cylinder: $[K_{supp}^{SB}, K_{supp}^{DBa}, K_{supp}^{DBb}, K_{supp}^{TB}] = [17, 12, 12, 17]$.

The target subspace size for target scattering coefficient linearization:

- Vertical cylinder: $[K_{scatt}^{SB}, K_{scatt}^{DBa}, K_{scatt}^{DBb}, K_{scatt}^{TB}] = [14, 14, 14, 14]$.
- Tilted cylinder: $[K_{scatt}^{SB}, K_{scatt}^{DBa}, K_{scatt}^{DBb}, K_{scatt}^{TB}] = [20, 20, 20, 20]$.

REFERENCES

1. Lu, D., “The potential and challenge of remote sensing-based biomass estimation,” *Int. Journal of Rem. Sens.*, Vol. 27, No. 7, 1297–1328, 2006.
2. Le Toan, T., S. Quegan, S. M. W. J. Davidson, H. Balzter, P. Paillou, K. Papathanassiou, S. Plummer, F. Rocca, S. Saatchi, H. Shugart, and others, “The BIOMASS mission: Mapping global forest biomass to better understand the terrestrial carbon cycle,” *Remote Sensing of Environment*, Vol. 115, No. 11, 2850–2860, 2011.
3. Cantaloube, H. and E. Colin Koeniger, “POLINSAR for FOPEN using flashlight mode images along circular trajectories,” *IEEE Int. Geosc. and Rem. Sens. Symposium*, 1139–1142, 2007.
4. Davis, M., *Foliage Penetration Radar: Detection and Characterization of Objects under Trees*, Scitech Publishing Inc., New York, 2011.
5. Lee, J. S. and E. Pottier, *Polarimetric Radar Imaging: From Basics to Applications*, CRC Press, 2009.
6. Treuhaft, R. N. and P. R. Siqueira, “Vertical structure of vegetated land surfaces from interferometric and polarimetric radar,” *Radio Science*, Vol. 35, No. 1, 141–177, 2000.
7. Treuhaft, R. N. and P. R. Siqueira, “The calculated performance of forest structure and biomass estimates from interferometric radar,” *Waves in Random Media*, Vol. 14, No. 2, S345–S358, 2004.
8. Treuhaft, R. N., B. E. Law, and G. P. Asner, *BioScience*, Vol. 54, No. 6, 561–571, 2004.
9. Li, Z., H. Wang, T. Su, and Z. Bao, “Generation of wide-swath and high-resolution SAR images from multichannel small spaceborne SAR systems,” *IEEE Geos. and Rem. Sens. Letters*, Vol. 2, No. 1, 82–86, 2005.
10. Huang, Y., L. Ferro-Famil, and C. Lardeux, “Polarimetric SAR tomography of tropical forests at P-band,” *IEEE Int. Geosc. and Rem. Sens. Symposium*, 1373–1376, 2011.
11. Minh, D. H. T., T. Le Toan, F. Rocca, S. Tebaldini, L. Villard, and others, “SAR tomography for the retrieval of forest biomass and height: Cross-validation at two tropical forest sites in French Guiana,” *Remote Sensing of Environment*, Vol. 175, 138–147, 2016.
12. Pardini, M., V. Cazcarra-Bes, and K. Papathanassiou, “TomoSAR mapping of 3D forest structure: Contributions of L-band configurations,” *Remote Sens.*, Vol. 13, No. 12, 2255, 2021.
13. Garestier, F., P. C. Dubois-Fernandez, D. Guyon, and T. Le Toan, “Forest biophysical parameter estimation using L- and P-band polarimetric SAR data,” *IEEE Trans. on Geosc. Rem. Sens.*, Vol. 47, No. 10, 3379–3388, 2009.
14. European Space Agency website, *Biomass Mission*, https://www.esa.int/Applications/Observing_the_Earth/The_Living_Planet_Programme/Earth_Explorers/Biomass, 2022.
15. Mermoz, S., M. Réjou-Méchain, L. Villard, T. Le Toan, V. Rossi, and S. Gourlet-Fleury, “Decrease of L-band SAR backscatter with biomass of dense forests,” *Remote Sensing of Environment*, Vol. 159, 307–317, 2015.

16. Ulaby, F. T., K. Sarabandi, K. McDonald, M. Whitt, and M. C. Dobson, "Michigan microwave canopy scattering model," *Int. Journal of Rem. Sens.*, Vol. 11, No. 7, 1223–1253, 1990.
17. Thirion, L., E. Colin Koeniger, and C. Dahon, "Capabilities of a forest coherent scattering model applied to radiometry, interferometry, and polarimetry at P- and L-band," *IEEE Trans. on Geosc. Rem. Sens.*, Vol. 44, No. 4, 849–862, 2006.
18. Bellez, S., C. Dahon, and H. Roussel, "Analysis of the main scattering mechanisms in forested areas: An integral representation approach for monostatic radar configurations," *IEEE Trans. on Geosc. Rem. Sens.*, Vol. 47, No. 12, 4153–4166, 2009.
19. Bellez, S., H. Roussel, C. Dahon, and J. M. Geffrin, "A rigorous forest scattering model validation through comparison with indoor bistatic scattering measurements," *Progress In Electromagnetics Research B*, Vol. 33, No. 7, 1–19, 2011.
20. Bellez, S., H. Roussel, C. Dahon, J. C. Castelli, and A. Cheraly, "Full polarimetric bistatic radar imaging experiments on sets of dielectric cylinders above a conductive circular plate," *IEEE Trans. on Geosc. Rem. Sens.*, Vol. 51, No. 7, 4164–4176, 2013.
21. Fenni, I., H. Roussel, M. Darces, and R. Mittra, "Fast analysis of large 3-D dielectric scattering problems arising in remote sensing of forest areas using the CBFM," *IEEE Trans. on Ant. and Prop.*, Vol. 62, No. 8, 4282–4291, 2014.
22. Fall, M., H. Roussel, C. Dahon, M. Casaletti, I. Fenni, and R. Mittra, "A high performance MPI implementation of numerical modeling of electromagnetic scattering from forest environment," *IEEE APURSI*, 2011–2012, 2016.
23. Sarabandi, K., *Electromagnetic Scattering from Vegetation Canopies*, Michigan University Press, 1989.
24. Ulaby, F. T., *Radar Polarimetry for Geoscience Applications*, Artech House, Inc., 1970.
25. Haupt, R. L. and S. Ellen Haupt, *Practical Genetic Algorithms*, Wiley Online Library, 2004.
26. Karam, M. A. and A. K. Fung, "Electromagnetic scattering from a layer of finite length, randomly oriented, dielectric, circular cylinders over a rough interface with application to vegetation," *Int. Journal of Rem. Sens.*, Vol. 9, No. 6, 1109–1134, 1988.